

## Article

# A Proportional-Integral-Resonant Current Control Strategy for a Wind-Driven Brushless Doubly Fed Generator during Network Unbalance

Defu Cai <sup>1</sup>, Haiguang Liu <sup>1</sup>, Sheng Hu <sup>2,\*</sup>, Guanqun Sun <sup>1</sup>, Erxi Wang <sup>1</sup> and Jinrui Tang <sup>2</sup> 

<sup>1</sup> State Grid Hubei Electric Power Research Institute, Wuhan 430064, China; caidf4@hb.sgcc.com.cn (D.C.); lhg071@126.com (H.L.); 15171506729@163.com (G.S.); wangex@hb.sgcc.com.cn (E.W.)

<sup>2</sup> School of Automation, Wuhan University of Technology, Wuhan 430074, China; tangjinrui@whut.edu.cn

\* Correspondence: hushee@whut.edu.cn

**Abstract:** This article proposes a proportional-integral-resonant (PIR) current control strategy for a wind-driven brushless doubly fed generator (WDBDFG) during network unbalance. Firstly, four control objectives of WDBDFG, including eliminating unbalanced currents of power winding (PW), pulsations of control winding (CW) currents, torque, and PW power, are discussed and different from current controls in which the references to PW currents were computed; the CW current references are derived here. Then, an improved CW current controller using a PIR controller is proposed to achieve different control objectives. In contrast with current controls, CW currents are not involved with sequence extraction in the proposed control and can be totally regulated only in a positive synchronous reference frame. Hence, the system control structure is greatly simplified, and dynamic characteristics are improved. Furthermore, in order to obtain completely decoupled control of current and average power, feedforward control, considering all the couplings and perturbances, is also applied in CW current loops. Simulation results for a 2 MW grid-connected WDBDFG show that the proposed control is capable of achieving four control objectives, including canceling CW current distortion, PW current unbalance, pulsations of PW active power or pulsations of reactive power, and machine torque. Its dynamic process is much more smoothly and quickly than that of current controls, and therefore the proposed control has better dynamic control characteristics during network unbalance.

**Keywords:** wind-driven brushless doubly fed generator (WDBDFG); network unbalance; proportional-integral-resonant (PIR) regulators; sequence extraction



**Citation:** Cai, D.; Liu, H.; Hu, S.; Sun, G.; Wang, E.; Tang, J. A

Proportional-Integral-Resonant Current Control Strategy for a Wind-Driven Brushless Doubly Fed Generator during Network Unbalance.

*Electronics* **2024**, *13*, 1616. <https://doi.org/10.3390/electronics13091616>

Academic Editor: Davide Astolfi

Received: 6 March 2024

Revised: 13 April 2024

Accepted: 17 April 2024

Published: 23 April 2024



**Copyright:** © 2024 by the authors. Licensee MDPI, Basel, Switzerland. This article is an open access article distributed under the terms and conditions of the Creative Commons Attribution (CC BY) license (<https://creativecommons.org/licenses/by/4.0/>).

## 1. Introduction

Nowadays, the utilization of wind energy has gained extensive concern all over the world. Because of their merits, such as decoupled control and small converter size, traditional doubly fed induction generator (DFIG)-based wind turbines have been popularly installed on wind farms over the past decades. Nevertheless, the DFIG's electric brushes and slip rings degrade system reliability and increase its maintenance cost [1–9]. By comparison, a new type of multiport electric machine, the brushless doubly fed generator (BDFG), not only inherits the advantages of traditional DFIG but also overcomes its aforementioned disadvantages, such as canceling the electric brushes and slip rings and having better low voltage ride-through (LVRT) capability [2–10]. Thus, the use of BDFG can greatly enhance the reliability of wind generation systems and lower their cost. It therefore has promising prospects in energy conversion applications. The operation of BDFG can be stand-alone [11–16] or grid-connected [1–9]. Usually, in stand-alone operation, the frequency and voltage are controlled for load, whereas in grid-connected operation, active and reactive power are adjusted according to the requirements of the power grid. In a wind generation system, the BDFG is usually driven by a wind turbine. The structure of

grid-connected, wind-driven BDFG (WDBDFG) is described in Figure 1. As described, the WDBDFG system consists of a wind turbine, gearbox, BDFG, grid-side converter (GSC), machine-side converter (MSC), and controllers. Among them, BDFG is composed of power winding (PW), control winding (CW), and a specially designed rotor winding (RW), which can be divided into rotor power winding (RPW) and rotor control winding (RCW).

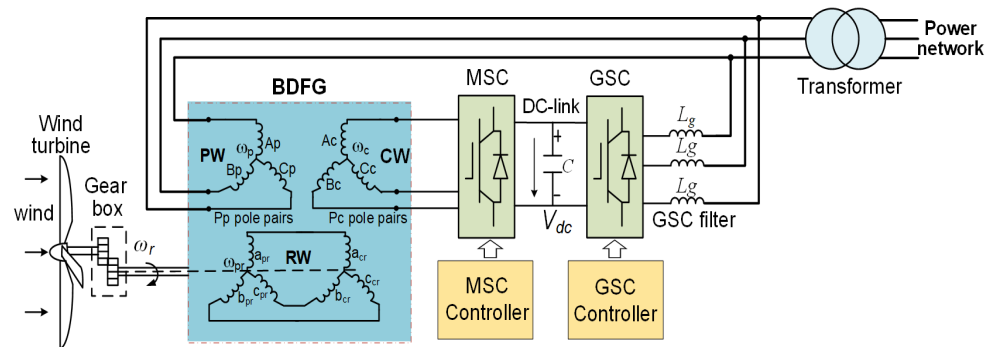


**Figure 1.** Structure of a grid-connected WDBDFG system.

The modeling and controls for BDFG-based generation systems under balanced networks have been well studied in [17–24]. Nevertheless, as shown in Figure 1, due to the direct connection between the PW of BDFG and the network, BDFG is very susceptible to network disturbances such as network voltage unbalance. The negative sequence component of unbalanced network voltages will lead to the unbalance of PW currents, distortions of RW and CW currents, pulsations of PW power, and machine torque [25–27]. These adverse effects have deleterious effects on WDBDFG and even lead to damage to its electrical and mechanical parts. Thus, it is very necessary to study the control methods for WDBDFG under network unbalance so as to improve the capability to resist the network unbalance. Thus far, the modeling and control for WDBDFG under network unbalance have been investigated in [25–29]. Nevertheless, the controls in [25,28,29] have similar drawbacks, including adopting a double-closed loop control structure, involving the decomposition of both CW and PW current sequence components, and the cross-coupling terms in control loops being totally or partially neglected. These drawbacks lead to a very complex control structure, and system-decoupled control is also affected. In addition, since it was not CW current references but the PW current references under different control objectives were deduced, a double-closed loop design was needed. In order to address the problems mentioned above, improved controls were proposed in [26,27], where a single-loop proportional-integral (PI) controller for CW current was proposed to realize the control objectives set. Moreover, because feedforward control was also applied in the CW loop by using all the disturbances and couplings deduced, decoupled control was also improved. Nevertheless, in [26,27], a dual PI controller including a positive and a negative sequence CW current controller was designed, and the extraction of positive and negative sequences of CW currents was still necessary. However, because the extraction process can introduce significant amplitude and phase errors, the dynamic response of CW current is affected, and CW current cannot realize fully decoupled control during the transient process. Furthermore, the multi-use of the decomposition algorithm also increases the complexity of the control structure. Additionally, for BDFG (MSC), only one control objective of canceling pulsations of torque and PW reactive power was discussed, and a corresponding control reference of CW current was deduced; other control objectives such as canceling pulsations of CW current, PW current unbalance, and PW active power pulsations were not studied.

The above problems in existing studies weakened the control capability of WDBDFG to resist network unbalance. To overcome these problems, an improved control strategy for WDBDFG under network unbalance is proposed in this paper. In the proposed control, a

proportional-integral-resonant (PIR) current controller composed of proportional, integral, and resonant regulators is designed. The main contributions include the following:

(1) For WDBDFG (MSC), apart from the control objective of canceling pulsations of torque and PW reactive power, another three control objectives, including eliminating pulsations of CW current, eliminating the unbalance of PW current, and eliminating pulsations of PW active power, are discussed. Furthermore, it was the CW current references but not the PW current references under different control objectives that were deduced. This provides a basis for the design of an improved PIR current controller with a single-closed loop structure.

(2) An improved single-loop CW current controller using a PIR regulator is designed to control CW current to track the references under network unbalance. Compared to the existing dual PI control, where the sequence extraction of CW current is necessary, in the proposed PIR control, CW currents are not involved with sequence extraction and can be totally regulated only in a positive synchronous reference frame. Hence, in contrast with current controls using a dual PI controller, the proposed control is greatly simplified, and dynamic characteristics are improved. Also, the proposed control is more applicable. Furthermore, in order to obtain completely decoupled control of current and average power, feedforward control using all the couplings and perturbances deduced is also applied in CW current loops.

Simulation tests for a 2 MW grid-connected WDBDFG verify that the proposed control is capable of achieving four control objectives and exhibits good stable and dynamic control characteristics under network unbalance.

## 2. Modeling of BDFG under Network Unbalance

Under an unbalanced network, the mathematical model of BDFG in a PW positive sequence synchronous  $(d_p q_p)^+$  rotary frame can be given as follows [14,15,26,27,29]:

$$v_{pdq}^+ = r_p i_{pdq}^+ + p \psi_{pdq}^+ + j \omega_p \psi_{pdq}^+ \quad (1)$$

$$v_{cdq}^+ = r_c i_{cdq}^+ + p \psi_{cdq}^+ + j \omega_c \psi_{cdq}^+ \quad (2)$$

$$v_{rdq}^+ = r_r i_{rdq}^+ + p \psi_{rdq}^+ + j \omega_{pr} \psi_{rdq}^+ \quad (3)$$

$$\psi_{pdq}^+ = L_p i_{pdq}^+ + L_{pr} i_{rdq}^+ \quad (4)$$

$$\psi_{cdq}^+ = L_c i_{cdq}^+ - L_{cr} i_{rdq}^+ \quad (5)$$

$$\psi_{rdq}^+ = L_r i_{rdq}^+ + L_{pr} i_{pdq}^+ - L_{cr} i_{cdq}^+ \quad (6)$$

where  $v_{pdq}^+$ ,  $v_{rdq}^+$ , and  $v_{cdq}^+$  represent voltage space vectors of PW, CW and RW in  $(d_p q_p)^+$  rotary reference frame, respectively;  $i_{pdq}^+$ ,  $i_{cdq}^+$ , and  $i_{rdq}^+$  represent current space vectors of PW, CW, and RW in  $(d_p q_p)^+$  rotary reference frame;  $\psi_{pdq}^+$ ,  $\psi_{cdq}^+$ , and  $\psi_{rdq}^+$  represent flux space vectors of PW, CW, and RW in  $(d_p q_p)^+$  rotary reference frame, respectively;  $r_p$ ,  $r_c$ ,  $r_r$ ,  $L_p$ ,  $L_c$ , and  $L_r$  represent resistance and self-inductance of PW, CW, and RW;  $L_{pr}$  and  $L_{cr}$  represent mutual inductance between PW and RW and CW and RW;  $p$  represents differential operator;  $\omega_p$ ,  $\omega_c$  and  $\omega_{pr}$  represent the frequency of PW, CW, and RPW, respectively;  $v_{rdq}^+ = 0$ ,  $\omega_c = \omega_p - (p_p + p_c)\omega_r$ ,  $\omega_{pr} = \omega_p - p_p\omega_r$ ;  $\omega_r$  represent rotor rotating speed;  $p_p$  and  $p_c$  represent the pole pairs of PW and CW, respectively; subscripts  $p$ ,  $c$ , and  $r$  represent PW, CW, and RW.

The spatial relationships of BDFG between  $\alpha_p \beta_p$  reference frame,  $\alpha_c \beta_c$  reference frame revolving at speed  $(p_p + p_c)\omega_r$ ,  $\alpha_r \beta_r$  reference frame revolving at speed  $p_p\omega_r$ ,  $(d_p q_p)^+$  reference frame revolving at speed  $\omega_p$ , and  $(d_p q_p)^-$  reference frame revolving at speed  $-\omega_p$  is shown in Figure 2. In Figure 2,  $\theta_p$  and  $\theta_r$  represent the position angle of the positive sequence of PW flux and rotor position angle, respectively.

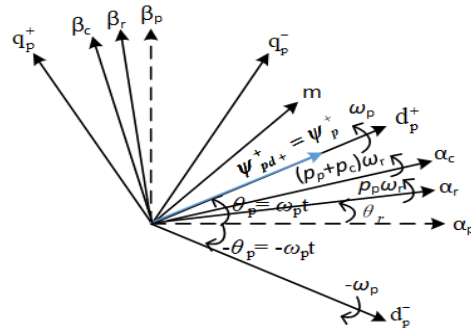


Figure 2. Relation between reference frames of  $(\alpha_p \beta_p)$ ,  $(\alpha_r \beta_r)$ ,  $(\alpha_c \beta_c)$ ,  $(dq)^+$ , and  $(dq)^-$ .

When network voltage is unbalanced, the physical quantities of BDFG can be extracted as positive and negative sequences. Thus, on the basis of Figure 2, the unbalanced space vectors  $m$ , including voltages, currents, and fluxes, are expressed in the  $(d_p q_p)^+$  rotary frame as follows:

$$m_{dq}^+ = m_{dq+}^+ + m_{dq-}^- e^{-j2\omega_p t} \tag{7}$$

where superscripts  $+$ ,  $-$  are  $(d_p q_p)^+$  and  $(d_p q_p)^-$  rational frames, and subscripts  $+$ ,  $-$  are positive and negative sequences.

In the  $(d_p q_p)^+$  rotary frame, according to (1)~(6), the CW voltage equation under network unbalance can be represented as follows [26,27]:

$$v_{cdq}^+ = r_c i_{cdq}^+ + \sigma L_c p i_{cdq}^+ + k_{cdq}^+ \tag{8}$$

where  $\sigma = 1 - L_{cr}^2 L_p / (L_{pr} L_M L_c)$ ,  $k_{cdq}^+$  denotes the perturbances and the couplings and can be written as follows:

$$k_{cdq}^+ = (j\omega_c L_c - j \frac{\omega_{pr} L_{cr}^2 L_p}{L_{pr} L_M}) i_{cdq}^+ + (j \frac{\omega_c L_{cr} L_p - \omega_{pr} L_{cr} L_p}{L_{pr}} - \frac{R_r L_p^2 L_{cr}}{L_{pr}^2 L_M}) i_{pdq}^+ + (-j \frac{\omega_c L_{cr}}{L_{pr}} + \frac{R_r L_p L_{cr}}{L_{pr}^2 L_M} + j \frac{\omega_{pr} L_{cr} L_p L_r}{L_{pr}^2 L_M}) \psi_{pdq}^+ \tag{9}$$

where  $L_M = (L_r L_p / L_{pr}) - L_{pr}$ .

Under network unbalance, the instantaneous active and reactive powers of PW and electromagnetic torque are represented as follows [26,27]:

$$\begin{aligned} P_p &= P_{p0} + P_{ps2} \sin 2\omega_p t + P_{pc2} \cos 2\omega_p t \\ Q_p &= Q_{p0} + Q_{ps2} \sin 2\omega_p t + Q_{pc2} \cos 2\omega_p t \\ T_{em} &= T_{em0} + T_{ems2} \sin 2\omega_p t + T_{emc2} \cos 2\omega_p t \end{aligned} \tag{10}$$

where  $P_{p0}$ ,  $P_{ps2}$ ,  $P_{pc2}$ ,  $Q_{p0}$ ,  $Q_{ps2}$ ,  $Q_{pc2}$ ,  $T_{em0}$ ,  $T_{ems2}$ , and  $T_{emc2}$  are the average values and the amplitudes of pulsation terms of PW active and reactive powers and electromagnetic torque, respectively, and can be given as follows:

$$\begin{bmatrix} P_{p0} \\ Q_{p0} \\ P_{ps2} \\ P_{pc2} \\ Q_{ps2} \\ Q_{pc2} \end{bmatrix} = -\frac{3L_r}{2L_M L_{pr}} \begin{bmatrix} v_{pd+}^+ & v_{pq+}^+ & v_{pd-}^- & v_{pq-}^- \\ v_{pq+}^+ & -v_{pd+}^+ & v_{pq-}^- & -v_{pd-}^- \\ v_{pq-}^- & -v_{pd-}^- & -v_{pq+}^+ & v_{pd+}^+ \\ v_{pd-}^- & v_{pq-}^- & v_{pd+}^+ & v_{pq+}^+ \\ -v_{pd-}^- & -v_{pq-}^- & v_{pd+}^+ & v_{pq+}^+ \\ v_{pq-}^- & -v_{pd-}^- & v_{pq+}^+ & -v_{pd+}^+ \end{bmatrix} \begin{bmatrix} \psi_{pd+}^+ \\ \psi_{pq+}^+ \\ \psi_{pd-}^- \\ \psi_{pq-}^- \end{bmatrix} + \frac{3L_{cr}}{2L_M} \begin{bmatrix} v_{pd+}^+ & v_{pq+}^+ & v_{pd-}^- & v_{pq-}^- \\ v_{pq+}^+ & -v_{pd+}^+ & v_{pq-}^- & -v_{pd-}^- \\ v_{pq-}^- & -v_{pd-}^- & -v_{pq+}^+ & v_{pd+}^+ \\ v_{pd-}^- & v_{pq-}^- & v_{pd+}^+ & v_{pq+}^+ \\ -v_{pd-}^- & -v_{pq-}^- & v_{pd+}^+ & v_{pq+}^+ \\ v_{pq-}^- & -v_{pd-}^- & v_{pq+}^+ & -v_{pd+}^+ \end{bmatrix} \begin{bmatrix} i_{cd+}^+ \\ i_{cq+}^+ \\ i_{cd-}^- \\ i_{cq-}^- \end{bmatrix} \tag{11}$$

$$\begin{bmatrix} T_{em0} \\ T_{ems2} \\ T_{emc2} \end{bmatrix} = \mu T_e \begin{bmatrix} -\psi_{pq+}^+ & \psi_{pd+}^+ & -\psi_{pq-}^- & \psi_{pd-}^- \\ \psi_{pd-}^- & \psi_{pq-}^- & -\psi_{pd+}^+ & -\psi_{pq+}^+ \\ -\psi_{pq-}^- & \psi_{pd-}^- & -\psi_{pq+}^+ & \psi_{pd+}^+ \end{bmatrix} \begin{bmatrix} i_{cd+}^+ \\ i_{cq+}^+ \\ i_{cd-}^- \\ i_{cq-}^- \end{bmatrix} \tag{12}$$

where

$$\mu_{Te} = \frac{3}{2} \left( \frac{p_c L_{cr} L_p L_r}{L_M L_{pr}^2} - \frac{p_c L_{cr}}{L_{pr}} - \frac{p_p L_{cr}}{L_M} \right)$$

### 3. Control Objectives for WDBDFG under Network Unbalance

Under network unbalance, according to (7), there exists unbalance in PW current and distortion in CW current, and according to (10), (11), and (12), there exist pulsations in electromagnetic torque and PW active and reactive powers, respectively. These adverse effects are very harmful to wind-driven BDFG, and power systems even lead to damage to BDFG’s electrical and mechanical parts and instability of the power system. Thus, in order to overcome these adverse effects and improve the control capability under network unbalance, the control objectives of WDBDFG can be designated as canceling CW current pulsations, keeping PW current balance, canceling pulsations of PW active and reactive powers, or machine torque pulsations, which are analyzed as follows:

**Control objective (1):** Canceling CW current pulsations, namely,  $i_{cd-}^- = i_{cq-}^- = 0$ . This control objective ensures that CW is heated evenly.

**Control objective (2):** Keeping PW current balance, namely,  $i_{pd-}^- = i_{pq-}^- = 0$ . This control objective ensures that PW is heated evenly.

**Control objective (3):** Canceling pulsations of PW active power, namely,  $P_{ps2} = 0$  and  $P_{pc2} = 0$ . In such instances, the MSC is controlled to cancel the pulsations in PW active power.

**Control objective (4):** Canceling pulsations of torque and PW reactive power, namely,  $T_{ems2} = 0$ ,  $T_{emc2} = 0$ ,  $Q_{ps2} = 0$ , and  $Q_{pc2} = 0$ . This control objective reduces the mechanical stress and cancels the pulsations in PW reactive power.

For the sake of simplifying the design of system control, the PW flux  $\psi_p^+$  oriented method can be adopted for WBDFG (MSC); therefore, as described in Figure 2, there are  $\psi_{pd+}^+ = \psi_p^+$ ,  $\psi_{pq+}^+ = 0$ . As a result, ignoring the smaller  $R_p$  and considering (7), Equation (1) can be simplified at steady state as follows:

$$\begin{aligned} v_{pdq+}^+ &= v_{pd+}^+ + jv_{pq+}^+ \approx j\omega_p \psi_{pdq+}^+ = j\omega_p \psi_{pd+}^+ \\ v_{pdq-}^- &= v_{pd-}^- + jv_{pq-}^- \approx -j\omega_p \psi_{pdq-}^- \end{aligned} \tag{13}$$

Control objective (1) requires  $i_{cdq-}^- = 0$ . As a result, according to (11) and (13), the positive and negative sequences of CW current reference are deduced as follows:

$$\begin{cases} i_{cd+}^* = \frac{2L_M Q_{p0}^*}{3L_{cr} v_{pq+}^+} + \frac{L_r (v_{pq+}^{+2} - v_{pd-}^{-2} - v_{pq-}^{-2})}{L_{pr} L_{cr} \omega_p v_{pq+}^+} \\ i_{cq+}^* = \frac{2L_M P_{p0}^*}{3L_{cr} v_{pq+}^+} \\ i_{cd-}^* = 0 \\ i_{cq-}^* = 0 \end{cases} \tag{14}$$

where  $P_{p0}^*$  and  $Q_{p0}^*$  are the active and reactive power references of PW.

Control objective (2) requires  $i_{pdq-}^- = 0$ . Using (4), RW current is derived as follows:

$$i_{rdq}^+ = \frac{\psi_{pdq}^+}{L_{pr}} - \frac{L_p}{L_{pr}} i_{pdq}^+ \tag{15}$$

Substituting (15) into (6) yields the following:

$$\psi_{rdq}^+ = \frac{L_r}{L_{pr}} \psi_{pdq}^+ - L_M i_{pdq}^+ - L_{cr} i_{cdq}^+ \tag{16}$$

By substituting (15) and (16) into (3), the RW voltage equation can be expressed as follows:

$$r_r \left( \frac{\psi_{pdq}^+ - L_p i_{pdq}^+}{L_{pr}} \right) + \frac{L_r}{L_{pr}} \frac{d\psi_{pdq}^+}{dt} - L_M \frac{di_{pdq}^+}{dt} - L_{cr} \frac{di_{cdq}^+}{dt} + j\omega_{pr} \left( \frac{L_r}{L_{pr}} \psi_{pdq}^+ - L_M i_{pdq}^+ - L_{cr} i_{cdq}^+ \right) = 0 \quad (17)$$

According to (17), by neglecting RW resistance  $R_r$  and transient processes, Equation (15) can be deduced as follows:

$$i_{cdq}^+ \approx \frac{L_r}{L_{pr} L_{cr}} \psi_{pdq}^+ - \frac{L_M}{L_{cr}} i_{pdq}^+ \quad (18)$$

Substituting  $i_{pdq-}^- = 0$  into (18) yields the following:

$$i_{cdq-}^- \approx \frac{L_r}{L_{pr} L_{cr}} \psi_{pdq-}^- \quad (19)$$

Hence, according to (11), (13), and (19), the required CW current reference is deduced as follows:

$$\begin{cases} i_{cd+}^{+*} = \frac{2L_M Q_{p0}^*}{3L_{cr} v_{pq+}^+} + \frac{L_r v_{pq+}^+}{L_{pr} L_{cr} \omega_p} \\ i_{cq+}^{+*} = \frac{2L_M P_{p0}^*}{3L_{cr} v_{pq+}^+} \\ i_{cd-}^{-*} = -\frac{L_r v_{pq-}^-}{L_{pr} L_{cr} \omega_p} \\ i_{cq-}^{-*} = \frac{L_r v_{pd-}^-}{L_{pr} L_{cr} \omega_p} \end{cases} \quad (20)$$

For *Control objective (3)*, by using (13) and substituting  $P_{ps2} = 0$  and  $P_{pc2} = 0$  into (11), the corresponding CW current reference can be deduced as follows:

$$\begin{cases} i_{cd+}^{+*} = \frac{2L_M v_{pq+}^+ Q_{p0}^*}{3L_{cr} (v_{pq+}^{+2} + v_{pd-}^{-2} + v_{pq-}^{-2})} + \frac{L_r v_{pq+}^+}{L_{pr} L_{cr} \omega_p} \\ i_{cq+}^{+*} = \frac{2L_M v_{pq+}^+ P_{p0}^*}{3L_{cr} (v_{pq+}^{+2} + v_{pd-}^{-2} - v_{pq-}^{-2})} \\ i_{cd-}^{-*} = -\frac{2L_r v_{pq-}^-}{L_{pr} L_{cr} \omega_p} + \frac{v_{pq-}^-}{v_{pq+}^+} i_{cd+}^{+*} - \frac{v_{pd-}^-}{v_{pq+}^+} i_{cq+}^{+*} \\ i_{cq-}^{-*} = \frac{2L_r v_{pq+}^+}{L_{pr} L_{cr} \omega_p} - \frac{v_{pd-}^-}{v_{pq+}^+} i_{cd+}^{+*} - \frac{v_{pq-}^-}{v_{pq+}^+} i_{cq+}^{+*} \end{cases} \quad (21)$$

For *Control objective (4)*, similarly, by using (13), substituting  $Q_{ps2} = 0$  and  $Q_{pc2} = 0$  into (11) or substituting  $T_{ems2} = 0$  and  $T_{emc2} = 0$  into (12), and PW power references into (11), the corresponding CW current reference can be deduced as follows [26,27]:

$$\begin{cases} i_{cd+}^{+*} = \frac{2L_M v_{pq+}^+ Q_{p0}^*}{3L_{cr} (v_{pq+}^{+2} - v_{pd-}^{-2} - v_{pq-}^{-2})} + \frac{L_r v_{pq+}^+}{L_{pr} L_{cr} \omega_p} \\ i_{cq+}^{+*} = \frac{2L_M v_{pq+}^+ P_{p0}^*}{3L_{cr} (v_{pq+}^{+2} + v_{pd-}^{-2} + v_{pq-}^{-2})} \\ i_{cd-}^{-*} = -\frac{v_{pq-}^-}{v_{pq+}^+} i_{cd+}^{+*} + \frac{v_{pd-}^-}{v_{pq+}^+} i_{cq+}^{+*} \\ i_{cq-}^{-*} = \frac{v_{pd-}^-}{v_{pq+}^+} i_{cd+}^{+*} + \frac{v_{pq-}^-}{v_{pq+}^+} i_{cq+}^{+*} \end{cases} \quad (22)$$

It is worthy of noting that, compared to controls in [26,27], apart from the control objective of canceling pulsation of machine torque and PW reactive power, another three control objectives, including eliminating oscillations of CW current, eliminating the unbalance of PW current, and eliminating oscillations of PW active power, are also discussed, and the corresponding CW current references are derived. Moreover, compared to controls in [25,28,29], it was CW current references but not PW current references under different

control objectives that were deduced; this provides a basis for the design of an improved PIR current controller with a single-closed loop structure.

#### 4. Proposed PIR CW Current Controller

For the purpose of realizing the control objectives under network unbalance, according to (14) and (20)–(22), the required CW current references of  $i_{cd+}^{+*}$ ,  $i_{cq+}^{+*}$ ,  $i_{cd-}^{-*}$  and  $i_{cq-}^{-*}$  can be obtained. As a consequence, the CW (MSC) current controller should be designed so that the measured CW currents are capable of tracking the required CW current references. Usually, a dual PI controller including a positive sequence current controller in the  $(d_pq_p)^+$  reference frame and a negative sequence current controller in the  $(d_pq_p)^-$  reference frame is employed [26,27,29]. Hence, the sequence extraction for CW currents was needed, but the sequence extraction can bring considerable time delays and amplitude errors to CW current, which would affect the decoupling control of CW current under transient conditions and further worsen the dynamic characteristics of the whole control system. Furthermore, the multi-use of the decomposition algorithm also increases the complexity of the control structure. Aiming at these problems, an improved single-loop CW current controller using a PIR regulator is designed to control CW current to track the references under network unbalance.

Under network unbalance, it can be seen from (7) that, in the  $(d_pq_p)^+$  reference frame, the CW (MSC) current is transformed into a positive sequence (DC value) plus a negative sequence ( $2\omega_p$  AC sinusoidal value). Theoretically, in order to eliminate steady-state errors, the DC value can be controlled using a PI regulator, while the AC sinusoidal value can be controlled using an R regulator at a resonant frequency of  $2\omega_p$ . Thus, in the  $(d_pq_p)^+$  reference frame, CW current can be precisely controlled by a PIR regulator without the need for sequence extraction. The differences between PI and PIR regulators can be summarized in Table 1.

**Table 1.** Differences between PI and PIR regulators.

Regulator	PI	PIR
Control input	DC input	DC plus sinusoidal input
CW current sequence extraction	Need	No need
Whole control structure	Complex	Simple

Based on previous analysis and (7) and (8), the PIR regulator for CW (MSC) current can be designed using feedback and feedforward controls as follows:

$$v_{cd}^{+*} = \left( k_p + \frac{k_i}{s} + \frac{k_r s}{s^2 + 2\omega_{ct}s + (2\omega_p)^2} \right) (i_{cd}^{+*} - i_{cd}^+) + k_{cd}^+ \tag{23}$$

$$v_{cq}^{+*} = \left( k_p + \frac{k_i}{s} + \frac{k_r s}{s^2 + 2\omega_{ct}s + (2\omega_p)^2} \right) (i_{cq}^{+*} - i_{cq}^+) + k_{cq}^+ \tag{24}$$

In (23) and (24),  $k_p$ ,  $k_i$ , and  $k_r$  denote the proportional, integral, and resonant coefficients of the proposed PIR current regulator;  $2\omega_p$  represents the resonant frequency determined by network frequency  $\omega_p$ ;  $\omega_{ct}$  represents the cut-off frequency used to adjust the sensitivity to frequency  $2\omega_p$ ;  $v_{cd}^{+*}$  and  $v_{cq}^{+*}$  represent the control references of CW voltages on the  $(d_p)^+$  and  $(q_p)^+$  axes; and  $k_{cd}^+$  and  $k_{cq}^+$  shown in (9) denote the terms used for feedforward control.

According to (8), (23), and (24), the proposed PIR CW current controller is depicted in Figure 3. On the basis of Figure 3, the bode diagrams of the closed-loop transfer function are depicted in Figure 4, where  $k_i = 3$ ,  $k_p = 20$ ,  $k_r = 400$ , and  $\omega_{ct} = 3$  rad/s. For comparison, Figure 4 shows the bode diagrams using PI and PIR controllers. As shown in Figure 4, there are larger amplitude and phase errors at the  $2\omega_p$  ( $200 \pi$  rad/s, 100 Hz) frequency signal for the CW closed-loop transfer function using the traditional PI regulator. By contrast, when a PIR regulator is used, there are nearly no amplitude or phase errors at the  $2\omega_p$  ( $200 \pi$  rad/s,

100 Hz) frequency signal. Figure 5 shows the bode diagrams of the CW current open-loop transfer function. As can be seen, crossover frequencies, the gain, and the phase margins of using PI and PIR controllers have little difference. Consequently, the system of using a PIR regulator is almost as stable as using a PI regulator.

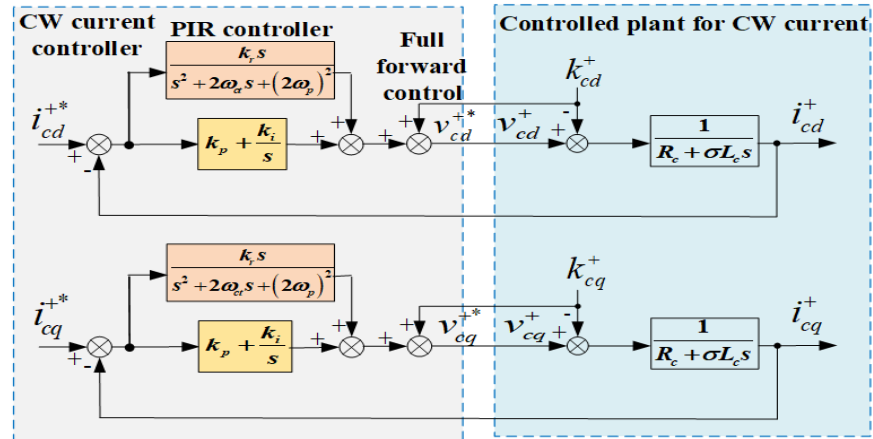


Figure 3. Block diagram of the proposed CW current controller.

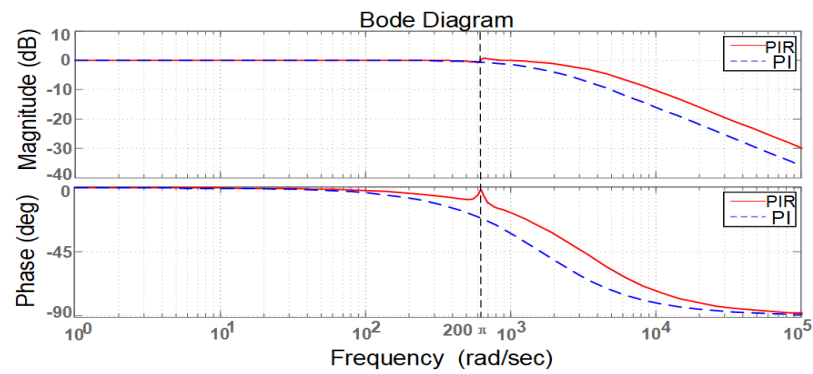


Figure 4. Bode diagrams of the CW current closed-loop transfer function with PIR and PI controllers.

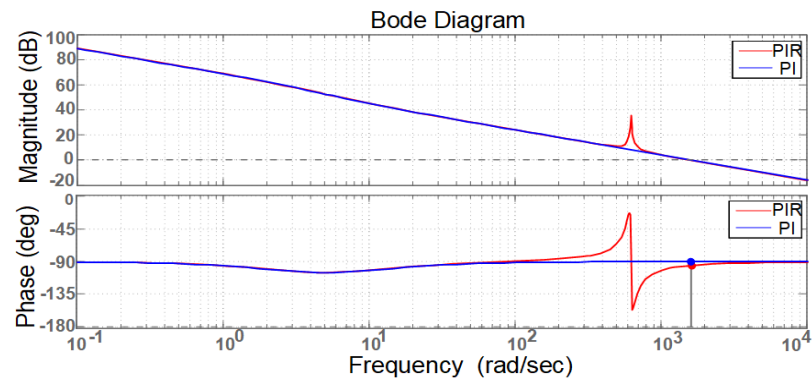


Figure 5. Bode diagrams of the CW current open-loop transfer function with PIR and PI controllers.

According to Figure 2 and Equation (7), the overall CW (MSC) control voltage in the CW stationary reference frame is deduced as follows:

$$v_{c\alpha\beta}^* = v_{cdq}^{+*} e^{j[\theta_p - (p_p + p_c)\theta_r]} \tag{25}$$

It should be noted that, in Figure 3, feedforward control using  $k_{cd}^+$  and  $k_{cq}^+$  is also applied in CW current loops so as to obtain completely decoupled control of current and average power. Moreover, it can be seen from (23)–(25) that the applicability of the

proposed strategy is limited by the maximum output voltage and current of MSC, i.e., the maximum capacity of MSC. Generally, the larger the MSC-rated capacity, the better the control capability of the proposed control, and the higher the network unbalance.

### 5. Whole Proposed Control Strategy

On the basis of Sections 3 and 4, the whole control strategy for grid-connected WDBDFG (MSC) under network unbalance is shown in Figure 6. As shown, under different control targets, the CW current references are directly computed by using (14) and (20)–(22), respectively. Furthermore, as analyzed before, in the CW current controller, after 3/2 and  $\alpha\beta/dq$  transformations, the measured CW currents are totally transformed into the  $(dq)$  reference frame, and obviously, they are not involved with sequence extraction. Then, controlled with PIR regulators, the CW control voltages  $v_{cd}^{+*}$  and  $v_{cq}^{+*}$  are outputted, and finally, after SVPWM modulation, the switch states for MSC are generated. Additionally, in Figure 6, for the purpose of calculating the references of CW current, sequence extraction for PW voltages and fluxes is required. Furthermore, a phase-locked loop (PLL) is required so as to fix the d+ axis on the positive sequence of PW flux revolving at the angular speed of  $\omega_p$ . There are various sequence extraction methods reported in the literature. Most of them make a tradeoff between accuracy and dynamic response. Comparatively, the multiple-complex coefficient-filter (MCCF)-based sequence extraction method in [30] has much better performance and, hence, is employed in the proposed control. With such an approach, the positive and negative sequences can be quickly and accurately extracted under network unbalance and distortion. Figure 7 illustrates the structural diagram of the MCCF-based PLL and sequence extraction method, where both  $\omega_c$  and  $\omega_1$  are equal to 314 rad/s.

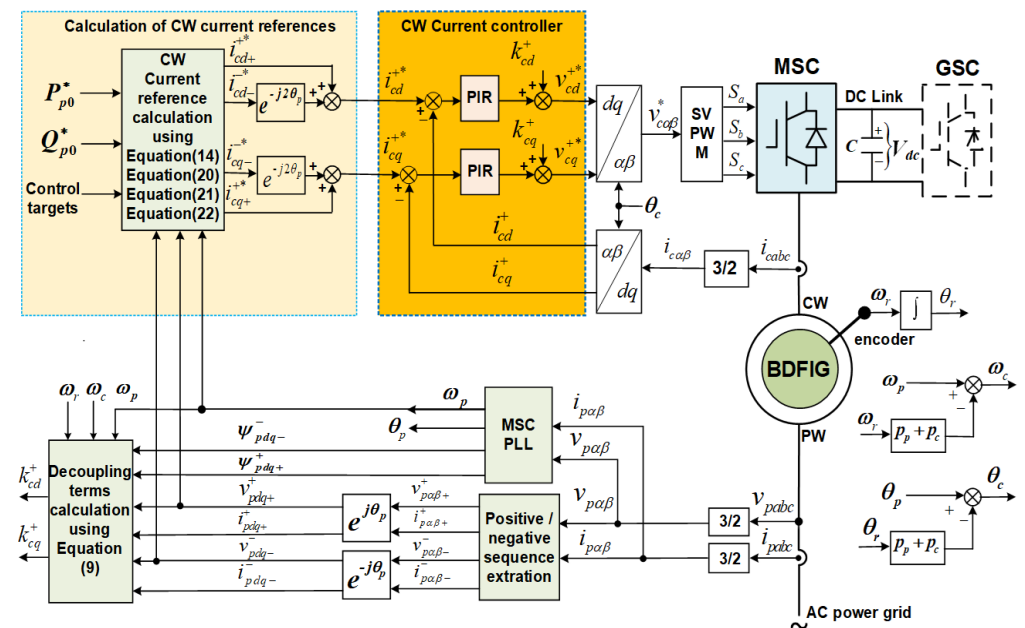
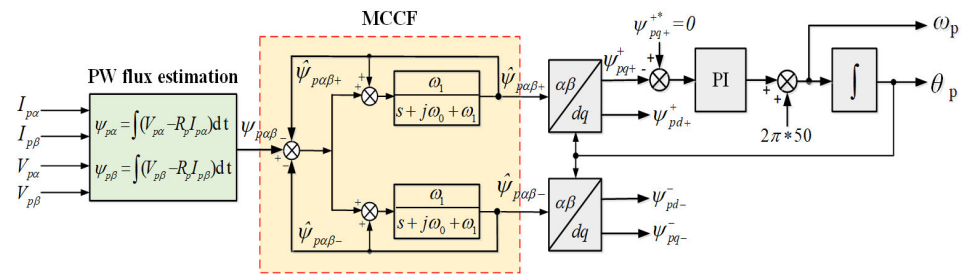


Figure 6. Whole proposed control strategy for grid-connected WDBDFG during network unbalance.



**Figure 7.** MCCF-based PLL and sequence extraction methods for MSC under network unbalance.

It is worth noting that the proposed control shown in Figure 6 is much simpler than existing controls. The improvement in the simplification of the control structure includes the following three aspects:

(1) In existing controls, a dual PI controller, including a positive and a negative sequence CW current controller, is usually designed. With a dual PI controller, a total of four positive and negative sequence components of CW current (positive sequence components on the d and q axes and negative sequence components on the d and q axes) are required to be controlled by using four PI regulators in two reference frames (positive and negative reference frames); hence, the parameters of the four PI regulators need to be tuned, and the structure of system control is very complex. In contrast, in the proposed control, a single PIR controller for CW current only in one reference frame (the positive reference frame) is designed. With the proposed control, the CW current (not its positive and negative sequence components) can be totally controlled just by using two PIR regulators in one reference frame (the positive reference frame).

(2) In existing controls, the decomposition algorithm for CW current is necessary. However, in the proposed control, the CW current can be totally controlled by using PIR regulators, and the decomposition algorithm for CW current is not required.

(3) In existing controls, usually a double-closed-loop control structure composed of a PW power or PW current outer loop and a CW current inner loop is designed. This is because the control references of CW current are not directly derived, and the output of the PW power or PW current outer loop is used as the control reference of the CW current inner loop. In contrast, in the proposed control, the control references of CW current are directly derived; therefore, a single-closed-loop control structure of CW current is enough, and a PW power or PW current outer loop is not required.

## 6. Simulation Verification

For the purpose of verifying the feasibility of the proposed control strategy, simulation tests for a WDBDFG system under network unbalance were implemented with Matlab-Simulink (software 7.8.0(R2009a)). The nominal power of WDBDFG is 2 MW, and its parameters are given in Table 2. This paper aims at the modeling and control of MSC (BDFG), and the controls of GSC have been investigated in [26,27]. Hence, here, it is assumed that the control objective for GSC is to maintain the voltage of the DC bus at 1200 V.

**Table 2.** Parameters of simulated WDBDFG.

Parameters	Values
Nominal power	2 MW
Nominal voltage	690 V
Nominal frequency	50 Hz
$r_p, r_c, r_r$ ( $\Omega$ )	0.0012, 0.0072, 0.0010
$L_p, L_c, L_r$ (mH)	3.1000, 6.8890, 19.050
$L_{pr}, L_{cr}$ (mH)	6.6560, 4.8940
Pole pairs ( $p_p, p_c$ )	2, 2

Figure 8 illustrates the waveforms under the constant revolving speed of 1.1 p.u. and 9% network unbalance, where four different control objectives analyzed in Section 3 are applied to MSC. The PW power reference  $P_{p0}^*$  and  $Q_{p0}^*$  were 1.0 p.u. and 0 MVar, respectively. The control objective of the MSC was originally selected as *Control objective (1)*, then changed to *Control objective (2)* at 0.2 s, *Control objective (3)* at 0.4 s, and finally *Control objective (4)* at 0.6 s. As illustrated in Figure 8c, during 0–0.2 s, CW currents have no pulsations. When *Control objective (2)* is applied at 0.2 s, the unbalance of PW current disappears immediately in Figure 8b. Similarly, as shown in Figure 8e, when *Control objective (3)* is designated at 0.4 s, the pulsations in PW active power cancel. Finally, when *Control objective (4)* is selected at 0.6 s, the pulsations of the generator’s torque and the reactive power of the PW disappear at the same time, which is clearly illustrated in Figure 8f,g, respectively. Moreover, according to Figure 8d,  $i_{cd}^+$ ,  $i_{cq}^+$ ,  $i_{cd}^+$  and  $i_{cq}^+$  all contain DC values plus 100 Hz pulsations;  $i_{cd}^+$  and  $i_{cq}^+$  track with the references  $i_{cd}^{+*}$  and  $i_{cq}^{+*}$  very well; this attributes to the PIR controller analyzed in Section 4. Additionally, as illustrated in Figure 8e,f, the actual average values of output PW active and reactive powers are 1.0 p.u. and 0 MVar, which also follows the references very well. The PW current ( $I_p$ ) unbalance, CW current ( $I_c$ ) percentage of 105 Hz harmonic relative to the 5 Hz fundamental component, 100 Hz pulsations in the PW active and reactive powers ( $P_p$ ,  $Q_p$ ), and generator’s torque are also summarized and compared in Table 3. Obviously, the results in Table 3 are consistent with the waveforms in Figure 8. Hence, it is evident from Figure 8 and Table 2 that the four selectable control objectives, including no CW current oscillations, balanced PW current, eliminating pulsations of PW active power, canceling the pulsations in electromagnetic torque, and output reactive power of PW, have been fully achieved, respectively.

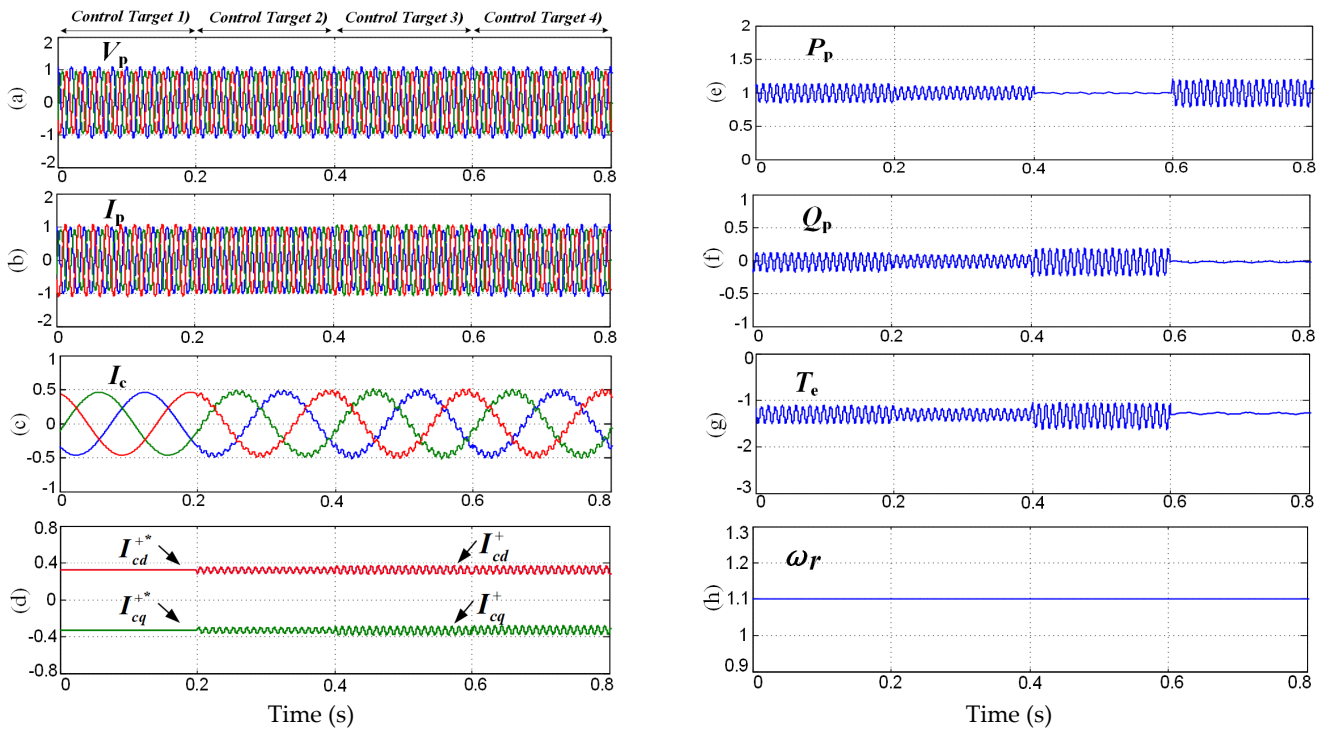


**Figure 8.** Waveforms for MSC with four control targets under 9% network unbalance ( $\omega_r = 1.1$  p.u.). (a) PW voltages (p.u.). (b) PW currents (p.u.). (c) CW currents (p.u.). (d) CW dq currents (p.u.). (e) PW active power (p.u.). (f) PW reactive power. (g) Electromagnetic torque (p.u.). (h) Rotor speed (p.u.).

**Table 3.** Comparison of four control targets.

Control Targets	(1)	(2)	(3)	(4)
$I_p$ unbalance (%)	3.02	1.01	3.53	4.22
$I_c$ distortion (%)	0.21	3.10	4.12	4.50
$P_p$ oscillation (%)	4.53	3.03	1.51	9.15
$Q_p$ oscillation (%)	5.12	3.52	8.83	1.87
$T_e$ oscillation (%)	3.96	2.91	8.11	2.25

Further study under the working condition of varied rotor speed from sub-synchronous state to super-synchronous state is also implemented by using the proposed control strategy. The PW active power reference  $P_{p0}^*$  is originally equal to 0.5 p.u., and at 1.4 s, it steps up from 0.5 p.u. to 1.0 p.u. The PW reactive power reference  $Q_{p0}^*$  is originally equal to  $-0.25$  p.u. (capacitive reactive power) and steps up from  $-0.25$  p.u. (capacitive reactive power) to 0.25 p.u. (inductive reactive power) at 1.6 s. Rotor rotary speed varies from 0.7 p.u. (sub-synchronous state) to 1.3 p.u. (super-synchronous state) during 0.2 s to 1.2 s. The network unbalance is 8.5%. Figure 9 illustrates the waveforms of variable rotor speed. Figure 10A,B illustrate the comparisons of the waveform with conventional vector control, where network unbalance is not considered, and the proposed control, respectively. In the proposed control, the control objective was originally selected as *Control objective (1)*, then changed into *Control objective (4)* at 0.5 s. As illustrated in Figure 10A(a,b), there exist severe unbalances in PW current and distortions in CW current. Moreover, as illustrated in Figure 10A(d–f), PW output active and reactive powers and generator torque all have large 100 Hz pulsations. By contrast, as illustrated in Figure 10B(a–c,f), when PW active power stepped up at 1.4 s, PW current, CW current, and electromagnetic torque also increased. Likewise, as illustrated in Figure 10B(b,c,e,f), during 0–0.5 s, the control objective of canceling oscillations of CW current is attained, and during 0.5–2 s, the control objective of canceling pulsations of reactive power and torque is realized as expected. Furthermore, as illustrated in Figure 10B(d,e), the control of PW active and reactive powers is decoupled and presents very good dynamic characteristics once again. Consequently, compared to conventional vector control, the proposed control is able to significantly enhance the capability of WDBDFG to resist network unbalance. In addition, as illustrated in Figure 9, when rotor speed is equal to 1.0 p.u. (i.e., the synchronous speed) at 0.7 s, it can be seen from Figure 10B(b,e,f) that at CW currents become DC current and *Control objective (4)* is achieved as expected; furthermore, nearby 0.7 s, CW currents are smoothly controlled to complete the change of phase sequence. Thus, at or near the synchronous state, the proposed control still shows good control performance. Figures 10 and 11A,B illustrate the spectrums of harmonics with conventional vector control and proposed control, respectively. As illustrated in Figure 11A(a–d), with conventional vector control, apart from fundamental frequency components, namely, 50 Hz in PW current and 15 Hz in CW current when  $\omega_r$  is 0.7 p.u., PW current also contains 150 Hz harmonics, and CW current mainly contains 85 Hz and 115 Hz harmonics. In addition, there are 100 Hz pulsations in both reactive power and the generator's torque. By contrast, it can be clearly seen from Figure 11B(a,b) that, when the proposed control is used and *Control objective (1)* is selected, the harmonics in PW and CW currents disappear. Moreover, according to Figure 11B(c,d), where *Control objective (4)* is selected, 100 Hz pulsations in reactive power and the generator's torque are eliminated at the same time. Consequently, the feasibility of the proposed control is verified again.

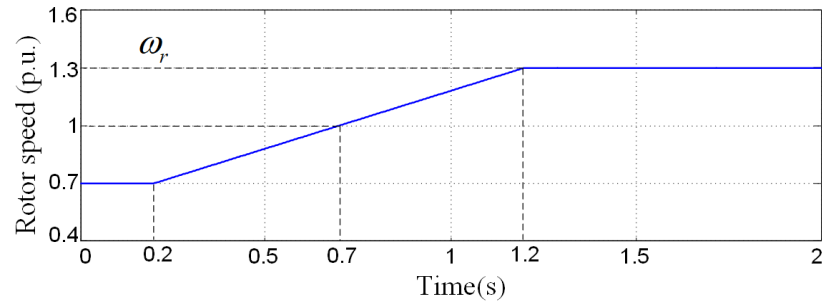


Figure 9. Waveforms of variable rotor rotating speed.

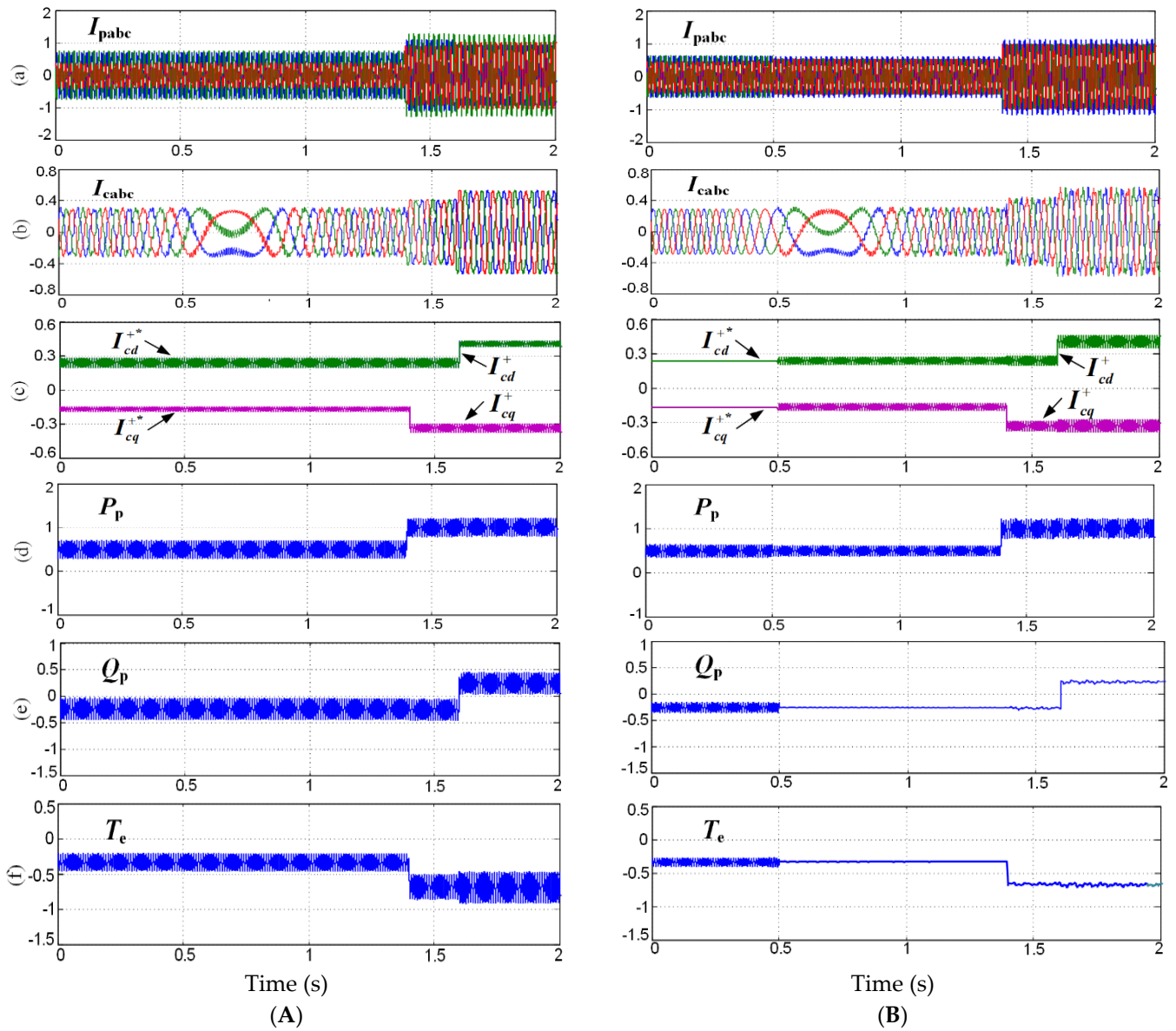
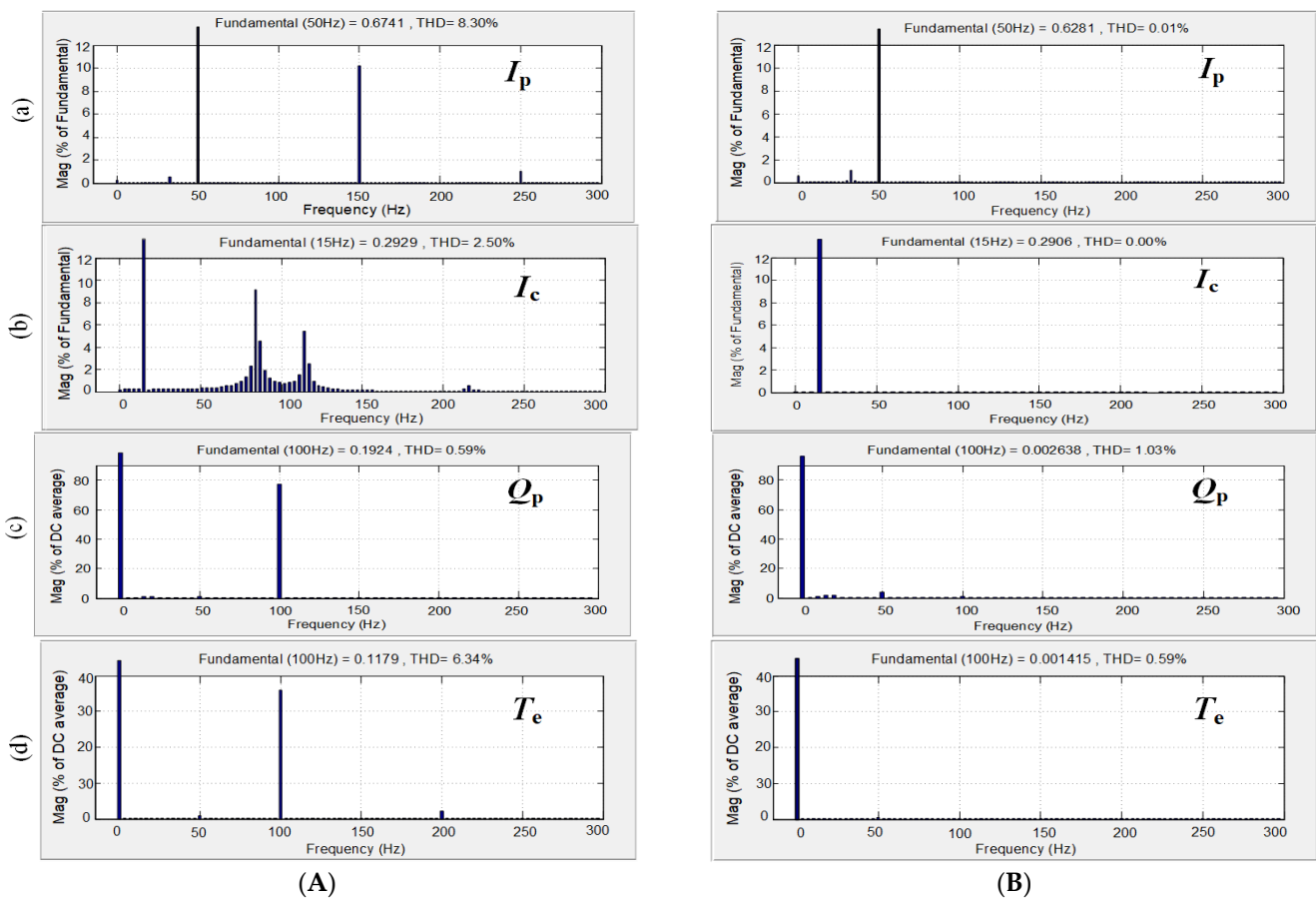


Figure 10. Waveforms with variations in rotor rotating speed under 8.5% network unbalance. (a) PW currents  $I_p$  (p.u.). (b) CW currents  $I_c$  (p.u.). (c) CW dq currents (p.u.). (d) PW active power  $P_p$  (p.u.). (e) PW reactive power  $Q_p$  (p.u.). (f) Electromagnetic torque  $T_e$  (p.u.). (A) Conventional vector control without consideration of network unbalance. (B) Proposed control.



**Figure 11.** Comparison of the harmonic spectrum based on the waveforms in Figure 9. (a) PW current. (b) CW current. (c) PW reactive power. (d) Electromagnetic torque. (A) Conventional vector control without consideration of network unbalance. (B) Proposed control.

In order to further test the improvements of the proposed control in dynamic performance, a study on the control of the WDBDFG system under transient network unbalance was also implemented. The transient network voltage unbalance of 9% appears at 0.4 s and disappears at 0.7 s; before 0.4 s and after 0.7 s, network voltage keeps balance. Two current controllers, namely, dual PI control in existing controls [26,27,29] and the proposed control, are compared, and the results are illustrated in Figure 12. Rotor rotary speed is kept at 1.1 p.u.; the power references  $P_{p0}^*$  and  $Q_{p0}^*$  were 1.0 p.u. and 0 MVar, respectively. The control objectives of both controls are set as *Control objective (4)*, i.e., canceling pulsations of torque and PW reactive power. Figure 12A illustrates the dynamic responses using the dual PI control in the existing control. In such control, the positive and negative sequence CW current controllers are designed. With a dual PI controller, a total of four positive and negative sequence components of CW current (positive sequence components on the d and q axes and negative sequence components on the d and q axes) are required to be controlled by using four PI regulators in two reference frames (positive and negative reference frames). Obviously, in order to obtain positive and negative sequence components of CW current, the decomposition algorithm for CW current is necessary. As illustrated in Figure 12A(a–c), from 0 s to 0.2 s, network unbalance voltage is balanced, and both  $I_{pabc}$  and  $I_{cabc}$  are balanced. When transient network unbalance appears during 0.2 s to 0.7 s,  $I_{pabc}$  and  $I_{cabc}$  become unbalanced and distorted. However, when network voltage returns to balance from 0.7 s to 1 s,  $I_{pabc}$  and  $I_{cabc}$  cannot return to balance in a short time but still remain unbalanced and distorted. Moreover, according to Figure 12A(d–f), when transient network unbalance appears during 0.2 s to 0.7 s, very large oscillations in  $Q_p$  and  $T_e$  appear and cannot be eliminated. Thus, *Control objective (4)* cannot be realized under

transient network unbalance with dual PI control. In addition, when network voltage returns to balance during 0.7 s to 1 s, very large oscillations in  $P_p$ ,  $Q_p$ , and  $T_e$  appear again and cannot disappear in a short time. According to testing results, dual PI control in existing controls presents poor dynamic performance. This is because sequence extractions of CW currents bring significant amplitude and phase errors to the control system, which affects the dynamic performances of CW currents and further worsens system dynamic characteristics. By comparison, Figure 12B illustrates the dynamic responses using the proposed control. As illustrated in Figure 12B(b–f), when network unbalance appears at 0.3 s and disappears at 0.7 s, the dynamic process is much more smoothly and quickly than that in Figure 12A(b)–B(f). Furthermore, according to Figure 12B(c,d), when network voltage returns to balance at 0.7 s,  $I_{pabc}$  and  $I_{cabc}$  return to balance quickly (the response time is approximately 5 ms). In addition, according to Figure 12A(d–f), during 0.2 s to 0.7 s, the oscillations in  $Q_p$  and  $T_e$  are small and eliminated in a short time (the response time is approximately 12 ms). Thus, *Control objective (4)* is totally achieved as expected. In addition, when network voltage returns to balance at 0.7 s, the oscillations in  $P_p$ ,  $Q_p$ , and  $T_e$  are also small and disappear quickly. In summary, the proposed control has much better dynamic performance than existing controls under network unbalance.

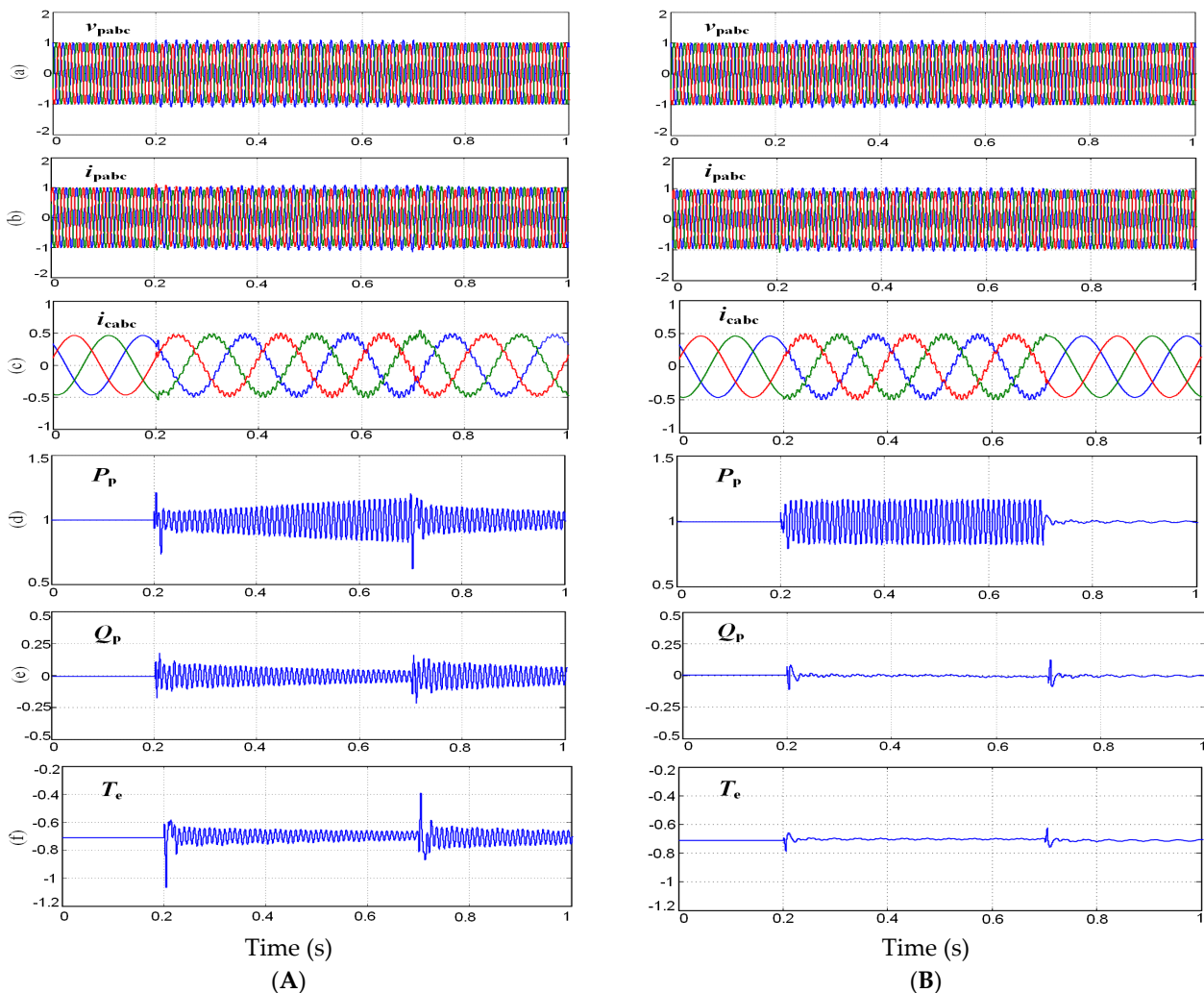


**Figure 12.** Comparison of two controls under 9% transient network unbalance during 0.2~0.7 s ( $\omega_r = 1.1$  p.u.). (a) Network voltage (p.u.). (b) PW currents (p.u.). (c) CW currents (p.u.). (d) PW active power (p.u.). (e) PW reactive power (p.u.). (f) Electromagnetic torque (p.u.). (A) Dual PI control. (B) Proposed control.

## 7. Conclusions

A PIR current control for WDBDFG during network unbalance was proposed in this article. Four selectable control objectives, including canceling PW current unbalance, pulsations of CW current, torque, and PW powers under network unbalance, are studied, and for the purpose of obtaining different control objectives, the CW current references were deduced but not the PW current references. This is the basis for the design of the proposed current controller with a single-closed loop structure. An improved single-loop CW current controller using PIR regulators is designed to control CW current to track the references under network unbalance. With the proposed control, CW currents are not involved with sequence extraction and can be totally regulated only in a positive synchronous reference frame. Hence, system control structure is significantly improved, and dynamic characteristics are improved. Additionally, in order to obtain completely decoupled control of current and average power, feedforward control using all the couplings and disturbances deduced is also applied in CW current loops. Simulation tests for a 2 MW grid-connected WDBDFG verify that the proposed control is capable of effectively achieving four control objectives and exhibits good stable and dynamic control characteristics under network unbalance.

**Author Contributions:** Conceptualization, D.C. and S.H.; methodology, D.C. and S.H.; validation, H.L. and S.H.; formal analysis, G.S.; investigation, E.W.; writing—original draft preparation, S.H.; writing—review and editing, S.H.; supervision, D.C. and J.T.; project administration, D.C. and J.T. All authors have read and agreed to the published version of the manuscript.

**Funding:** This work was supported by the Guidelines Project of the State Grid Corporation of China (grant numbers 5100-202199536A-0-5-ZN).

**Data Availability Statement:** The data presented in this study are available in this article.

**Conflicts of Interest:** Authors Defu Cai, Haiguang Liu, Guanqun Sun and Erxi Wang were employed by the company State Grid Hubei Electric Power Research Institute. The remaining authors declare that the research was conducted in the absence of any commercial or financial relationships that could be construed as a potential conflict of interest.

## References

1. Sadeghi, R.; Madani, S.M.; Lipo, T.A.; Kashkooli, M.R.A.; Ataei, M.; Ademi, S. Voltage dip analysis of brushless doubly fed induction generator using reduced T-model. *IEEE Trans. Ind. Electron.* **2019**, *11*, 991–1000. [[CrossRef](#)]
2. Strous, T.D.; Polinder, H.; Ferreira, J.A. Brushless doubly-fed induction machines for wind turbines: Developments and research challenges. *IET Electr. Power Appl.* **2017**, *11*, 991–1000. [[CrossRef](#)]
3. Gowaid, I.A.; Abdel-Khalik, A.S.; Massoud, A.M.; Ahmed, S. Ride through capability of grid-connected brushless cascade DFIG wind turbines in faulty grid conditions—A comparative study. *IEEE Trans. Sustain. Energy* **2013**, *4*, 1002–1015. [[CrossRef](#)]
4. Tohidi, S.; Tavner, P.; McMahan, R.; Oraee, H.; Zolghadri, M.R.; Shao, S.; Abdi, E. Low voltage ride-through of DFIG and brushless DFIG: Similarities and differences. *Electr. Power Syst. Res.* **2014**, *110*, 64–72. [[CrossRef](#)]
5. Gholizadeh, M.; Oraee, A.; Tohidi, S.; Oraee, H.; McMahan, R. An analytical study for low voltage ride through of the brushless doubly-fed induction generator during asymmetrical voltage dips. *Renew. Energy* **2018**, *115*, 64–75. [[CrossRef](#)]
6. Huang, J.; Li, S. Analytical expression for LVRT of BDFIG with enhanced current control to CW and reactive power support from GSC. *Int. J. Electr. Power Energy Syst.* **2018**, *98*, 243–255. [[CrossRef](#)]
7. Xu, J.; Nie, P. Optimal Control of Brushless Doubly Fed Wind Power Generator under Zero-Voltage Ride-Through. *Energies* **2024**, *17*, 235. [[CrossRef](#)]
8. Gholizadeh, M.; Tohidi, S.; Oraee, A.; Oraee, H. Appropriate crowbar protection for improvement of brushless DFIG LVRT during asymmetrical voltage dips. *Int. J. Electr. Power Energy Syst.* **2018**, *95*, 64–75. [[CrossRef](#)]
9. Lu, M.; Chen, Y.; Zhang, D.; Su, J.; Kang, Y. Virtual Synchronous Control Based on Control Winding Orientation for Brushless Doubly Fed Induction Generator (BDFIG) Wind Turbines Under Symmetrical Grid Faults. *Energies* **2019**, *12*, 319. [[CrossRef](#)]
10. Chen, X.; Pan, W.; Wang, X.; Zhou, Y. Design of a brushless doubly fed generator with simplified three-phase wound rotor. *IEEE Trans. Ind. Electron.* **2023**, *70*, 4427–4439. [[CrossRef](#)]
11. Hussien, M.; Liu, Y.; Xu, W.; Ismail, M. Voltage regulation-based sensorless position observer with high-frequency signal injection topology for BDFIGs in ship power microgrid systems. *Int. J. Electr. Power Energy Syst.* **2022**, *140*, 108091. [[CrossRef](#)]
12. Zhou, M.; Su, H.; Liu, Y.; Cai, W.; Xu, W.; Wang, D. Full-Order Terminal Sliding-Mode Control of Brushless Doubly Fed Induction Generator for Ship Microgrids. *Energies* **2021**, *14*, 7302. [[CrossRef](#)]
13. Cheng, M.; Jiang, Y.; Han, P.; Wang, Q. Unbalanced and low-order harmonic voltage mitigation of stand-alone dual-stator brushless doubly fed induction wind generator. *IEEE Trans. Ind. Electron.* **2018**, *65*, 9135–9146. [[CrossRef](#)]

14. Xu, W.; Mohammed, O.; Mohammed, E.; Liu, Y.; Rabiul, I. Negative sequence voltage compensating for unbalanced standalone brushless doubly-fed induction generator. *IEEE Trans. Power Electron.* **2020**, *35*, 667–680. [[CrossRef](#)]
15. Liu, Y.; Xu, W.; Zhu, J.; Blaabjerg, F. Sensorless control of standalone brushless doubly fed induction generator feeding unbalanced loads in a ship shaft power generation system. *IEEE Trans. Ind. Electron.* **2019**, *66*, 739–749. [[CrossRef](#)]
16. Liu, Y.; Xu, W.; Long, T.; Blaabjerg, F. An improved rotor speed observer for standalone brushless doubly-fed induction generator under unbalanced and nonlinear Loads. *IEEE Trans. Power Electron.* **2020**, *35*, 775–788. [[CrossRef](#)]
17. Han, P.; Cheng, M.; Wei, X.; Li, N. Modeling and performance analysis of a dual-stator brushless doubly fed induction machine based on spiral vector theory. *IEEE Trans. Ind. Appl.* **2016**, *52*, 1380–1389. [[CrossRef](#)]
18. Poza, J.; Oyarbide, E.; Sarasola, I.; Rodriguez, M. Vector control design and experimental evaluation for the brushless doubly fed machine. *IET Electr. Power Appl.* **2009**, *3*, 247–256. [[CrossRef](#)]
19. Shao, S.; Abdi, E.; Barati, F.; McMahon, R. Stator-flux-oriented vector control for brushless doubly fed induction generator. *IEEE Trans. Ind. Electron.* **2009**, *56*, 4220–4228. [[CrossRef](#)]
20. Protsenko, K.; Xu, D. Modeling and control of brushless doubly-fed induction generators in wind energy applications. *IEEE Trans. Power Electron.* **2008**, *23*, 1191–1197. [[CrossRef](#)]
21. Basic, D.; Zhu, J.G.; Boardman, G. Transient performance study of a brushless doubly fed twin stator induction generator. *IEEE Trans. Energy Convers.* **2003**, *18*, 400–408. [[CrossRef](#)]
22. Huerta, H.; Loukianov, A. Energy based sliding mode control of Brushless Double-fed Induction Generator. *Int. J. Electr. Power Energy Syst.* **2021**, *130*, 107002. [[CrossRef](#)]
23. Cárdenas, R.; Pena, R.; Wheeler, P.; Clare, J.; Munoz, A.; Sureda, A. Control of a wind generation system based on a Brushless Doubly-Fed Induction Generator fed by a matrix converter. *Electr. Power Syst. Res.* **2013**, *103*, 49–60. [[CrossRef](#)]
24. Zeng, Y.; Cheng, M.; Wei, X.; Xu, L. Dynamic modeling and performance analysis with iron saturation for dual-stator brushless doubly fed induction generator. *IEEE Trans. Energy Convers.* **2020**, *35*, 260–270. [[CrossRef](#)]
25. Shao, S.; Long, T. Dynamic control of the brushless doubly fed induction generator under unbalanced operation. *IEEE Trans. Ind. Electron.* **2013**, *60*, 2465–2476. [[CrossRef](#)]
26. Hu, S.; Zhu, G.; Kang, Y. Modeling and coordinated control design for brushless doubly-fed induction generator based wind turbine to withstand grid voltage unbalance. *IEEE Access* **2021**, *36*, 63331–63344. [[CrossRef](#)]
27. Hu, S.; Zhu, G. Enhanced control and operation for brushless doubly-fed induction generator based wind turbine under grid voltage unbalance. *Electr. Power Syst. Res.* **2022**, *207*, 117861. [[CrossRef](#)]
28. Chen, J.; Zhang, W.; Chen, B.; Ma, Y. Improved vector control of brushless doubly fed induction generator under unbalanced grid conditions for offshore wind power generation. *IEEE Trans. Energy Convers.* **2016**, *31*, 293–303. [[CrossRef](#)]
29. Xu, L.; Cheng, M.; Wei, X.; Yan, X.; Zeng, Y. Dual synchronous rotating frame current control of brushless doubly fed induction generator under unbalanced network. *IEEE Trans. Ind. Electron.* **2021**, *36*, 6712–6724. [[CrossRef](#)]
30. Guo, X.; Wu, W.; Chen, Z. Multiple-complex coefficient-filter-based phase-locked loop and synchronization technique for three-phase-grid-interfaced converters in distributed utility networks. *IEEE Trans. Ind. Electron.* **2011**, *58*, 1194–1204. [[CrossRef](#)]

**Disclaimer/Publisher’s Note:** The statements, opinions and data contained in all publications are solely those of the individual author(s) and contributor(s) and not of MDPI and/or the editor(s). MDPI and/or the editor(s) disclaim responsibility for any injury to people or property resulting from any ideas, methods, instructions or products referred to in the content.